minerals

MDPI

Article

Lithological and Structural Interpretation of Airborne Gamma-Ray Uranium Anomalies for Exploration: A Case Study from the Longshoushan Metallogenic Belt, China

Jianchun Xu, Yaohui Mi *, Yanxu Liu *, Baodi Wang, Zuoxi Jiang, Xuanjie Zhang, Yanan Zhang and Xin Wang

China Aero Geophysical Survey and Remote Sensing Center for Natural Resources, China Geological Survey, Beijing 100083, China; xujianchun@mail.cgs.gov.cn (J.X.)

* Correspondence: miyaohui@mail.cgs.gov.cn (Y.M.); liuyanxu@mail.cgs.gov.cn (Y.L.)

Abstract

To improve the geological constraints on regional screening for alkali-metasomatic uranium deposits, we analysed high-resolution airborne gamma-ray spectrometric data from the Xinshuijing–Yushigou area of the Longshoushan metallogenic belt, integrating ground gamma-ray spectrometry, geological zoning, fault structures, and drill-hole geological sections from the Xinshuijing and Jiling deposits. We assessed the lithological dependence of K, equivalent uranium (eU), equivalent thorium (eTh), and total count (TC), and developed a multi-parameter interpretation framework comprising the expected uranium background (Gu), relative uranium deviation (Hu), U–K relative enhancement index (F), and normalized relative uranium deviation (B). The regional radioelement distribution is primarily controlled by granitic intrusions and parts of the pre-Sinian metamorphic basement. However, the spatial extent of several local anomalies does not fully coincide with lithological boundaries, indicating variations in radioelement proportions superimposed on the lithological background. Drill-hole sections from Xinshuijing and Jiling show that known ore bodies and mineralized zones occur within granitic–dioritic rock associations and structurally controlled alteration zones. Their surface-projection neighbourhoods are characterized by a combination of high radioactive backgrounds, locally negative Hu values, enhanced F values, and adjacent positive relative uranium deviations. This correspondence improves the geological interpretability of the multi-parameter anomalies, although it represents retrospective validation using known deposits. Yushigou exhibits a similar parameter assemblage near the contact between a granitic intrusion and a NW-trending fault and is therefore identified as a candidate exploration target requiring independent field verification. These results demonstrate that decomposing absolute radiometric responses into lithological background, relative uranium deviation, and K–U–Th ratio variations helps identify local radioelement decoupling within regionally elevated radioactive backgrounds, providing complementary near-surface evidence for regional screening of concealed uranium mineralization in complex bedrock terrains.

Keywords: airborne gamma-ray spectrometry; alkali-metasomatic uranium deposits; Longshoushan metallogenic belt; concealed-ore prospectivity prediction

Check for updates

Academic Editor: Amin Beiranvand Pour

Received: 13 August 2026
Revised: 22 September 2026
Accepted: 23 September 2026
Published: 26 September 2026

Copyright: © 2026 by the authors. Licensee MDPI, Basel, Switzerland. This article is an open access article distributed under the terms and conditions of the Creative Commons Attribution (CC BY) license.

1. Introduction

Uranium resources underpin the sustainable development of nuclear energy, yet identifying concealed ore bodies within mature metallogenic belts remains a major challenge

to continued resource development. Alkali-metasomatic uranium deposits commonly occur in granitic rocks or metamorphic basement that have undergone multiple episodes of tectonic activity. Their formation is closely associated with regional faulting, alkaline-fluid migration, and metasomatic alteration, particularly albitization and hematitization [1–4]. The Longshoushan metallogenic belt, located along the southwestern margin of the North China Craton, is a representative alkali-metasomatic uranium province in China. It hosts several uranium deposits, including Xinshuijing and Jiling, and retains considerable potential for deep and peripheral exploration [5–8]. As exposed deposits and strong radioactive anomalies have progressively been investigated, regional exploration has shifted from conspicuous surface anomalies towards concealed mineral systems beneath cover or within areas characterized by subtle exploration signals [9–14].

Alkali-metasomatic uranium mineralization involves a multistage process in which uranium is mobilized from potential source regions, transported through structurally controlled fluid pathways, and subsequently re-enriched at favourable sites. The Longshoushan area has undergone multiple episodes of tectonic deformation, magmatism, and hydrothermal overprinting. The regional metamorphic basement comprises the Longshoushan Group, including marble, schist, gneiss, and migmatite, as outlined in Section 2.1. Its lithological variability may influence the regional radiometric background. Variations in redox conditions, fluid mixing, and metasomatic intensity may have further governed uranium mobilization and precipitation [15,16]. Consequently, high eU responses may represent either primary U-rich lithologies or later hydrothermal uranium addition, whereas low eU responses may indicate either an initially U-poor background or relative uranium depletion. Single-element radiometric responses alone therefore cannot reliably distinguish lithological background, potential migration pathways, and subsequent enrichment, resulting in non-unique interpretations of concealed exploration targets [17–20].

Airborne gamma-ray spectrometry provides spatially continuous measurements of near-surface potassium (K), equivalent uranium (eU), and equivalent thorium (eTh), and is widely used in regional geological mapping, alteration detection, and uranium exploration [21–24]. However, airborne radiometric responses originate predominantly from shallow surface materials and are affected by lithological composition, weathering and erosion, unconsolidated cover, topographic relief, and instrumental calibration [25]. In lithologically complex terrains affected by multiple hydrothermal events, different geological processes may produce similar radiometric signatures, while the same process may generate anomalies of different magnitudes. Absolute radiometric responses, background estimates, and relative deviations must therefore be distinguished explicitly to avoid interpreting intrinsically radioactive lithologies, lithological-boundary effects, or near-surface environmental variations directly as mineralization-related anomalies [26–32].

Thorium is generally less mobile than uranium in many hydrothermal environments and is therefore commonly used as a reference for estimating the lithological radiometric background. Nevertheless, the validity of this assumption may be affected by the mineralogical composition of the protolith, intense weathering, redistribution of Th-bearing minerals, and measurement uncertainty. Uranium is more sensitive to redox conditions and fluid–rock interaction. Its positive or negative deviation from the lithological background can thus describe relative increases or decreases in present-day near-surface eU, but cannot independently constrain the direction of uranium transport. Normalized parameters such as K/Th can help reduce lithological effects and identify potassic alteration [33,34]. Anomaly interpretation requires both the separation of anomalous responses from the geological background and validation against independent exploration evidence. Previous studies have optimized thresholds for distinguishing geochemical anomalies from background [35] and integrated magnetic-anomaly interpretation with geological observations

and subsequent drilling verification [36]. Although these studies used different exploration datasets, they demonstrate the importance of explicit anomaly-selection criteria and independent validation in mineral exploration. Although single-element concentrations, elemental ratios, and alteration indices have been widely applied to airborne gamma-ray spectrometric interpretation, the high-radioactivity bedrock setting of Longshoushan still lacks a systematic assessment of how to establish a reproducible lithological baseline, evaluate the stability of derived parameters, and distinguish increased interpretive information from genuine improvements in predictive performance [37–40].

Previous radiometric studies have used elemental ratios such as eU/eTh, eU/K, and eTh/K to enhance contrasts in radioelement distributions and assist the interpretation of lithology, weathering, alteration, and mineralization [41,42]. Thorium-referenced normalization, lithological-background correction, and derived uranium-deviation parameters have also been applied to reduce the influence of regional or lithological background on uranium-anomaly identification [43–45]. The F parameter, expressed as $F = K(eU/eTh)$, has been used as a composite measure of radioelement proportions and as a potential indicator of hydrothermal alteration, although its interpretation is inherently non-unique because it may increase in response to elevated K, elevated eU, decreased eTh, or combinations of these changes [44,45]. The present study builds on these established approaches rather than introducing four mathematically independent indicators. Its contribution lies in estimating the expected uranium background separately for mapped lithological units and jointly interpreting the resulting background levels, uranium deviations, and radioelement proportions in the Longshoushan metallogenic belt. Ground radiometric measurements and drill-hole geology provide complementary geological constraints for evaluating the observed near-surface patterns. The framework is intended to support exploration screening, and its predictive advantage over conventional radiometric interpretation remains to be evaluated using independent prospective targets.

This study uses high-resolution airborne gamma-ray spectrometric data acquired in 2022 over the Xinshuijing–Yushigou area of the Longshoushan metallogenic belt. These data are integrated with ground gamma-ray spectrometry, lithological zoning, fault information, and drill-hole geological sections from the Xinshuijing and Jiling deposits to establish a lithology-constrained, multi-parameter interpretation framework. We first characterize variations in K, eU, eTh, and total count (TC) among geological units. The expected uranium background (Gu) is then estimated from the relationship between eTh and lithological background, from which the relative uranium deviation (Hu), U–K relative enhancement index (F), and normalized relative uranium deviation (B) are calculated. Drill-hole sections from known deposits are subsequently used to retrospectively evaluate the spatial relationships between surface parameter assemblages and ore bodies, host rocks, dykes, and altered rocks. Xinshuijing and Jiling are used to assess the geological plausibility of these parameter assemblages, whereas Yushigou is treated as a candidate area for evaluating anomalous characteristics and alternative interpretations. The study examines whether multi-parameter maps provide reproducible information on lithological backgrounds and relative deviations beyond that available from eU alone, and uses this framework to identify candidate exploration targets for subsequent ground investigation.

2. Regional Geology and Metallogenic Setting

2.1. Regional Tectono-Stratigraphic Framework

The study area lies at the tectonic junction between the southern margin of the Alxa Block and the northern margin of the North Qilian Orogenic Belt. It is principally situated within the NW–SE-trending Longshoushan uplift belt (Figure 1). Multistage convergence, terrane accretion, and intracontinental reworking among the North China Craton, the

Alxa Block, and the Qilian Orogenic Belt produced a structural framework comprising regional deep-seated faults, subsidiary faults, and distinct basement units [46–49]. This framework controlled the spatial distribution of stratigraphic units and intrusive bodies and provided favourable conditions for subsequent hydrothermal activity and uranium redistribution [50–52].

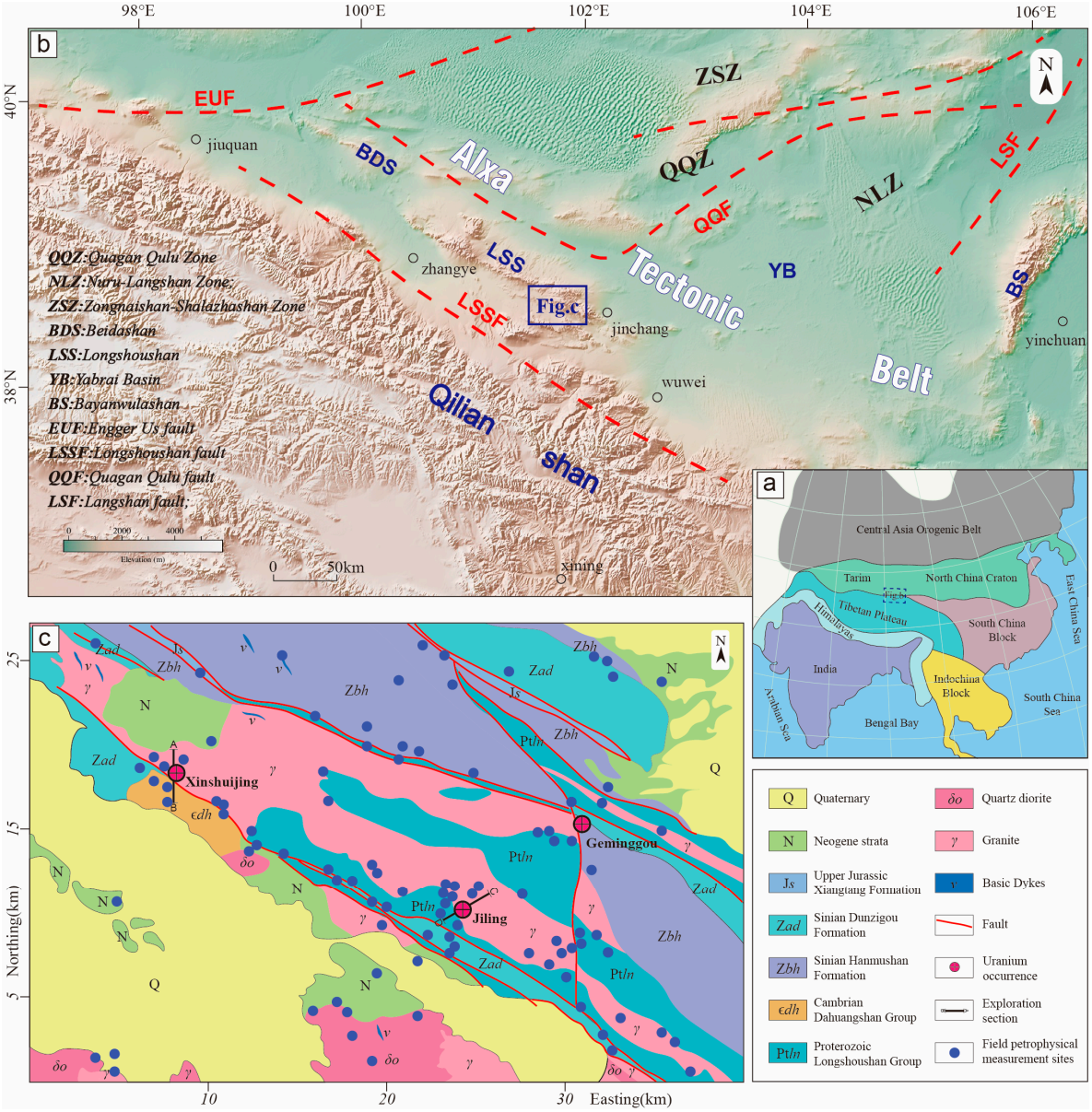

Figure 1. Geological setting of the study area. (**a**) Regional tectonic framework of the Central Asian Orogenic Belt [46,47]; the outlined box indicates the extent of panel (**b**). (**b**) Regional tectonic map [48]; the outlined box indicates the extent of panel (**c**). (**c**) Geological map of the study area showing lithological units, faults, uranium occurrences, exploration sections, and ground radiometric measurement sites [49].

The principal exposed stratigraphic units include the Paleoproterozoic Longshoushan Group, the Mesoproterozoic Dunzigou Group, and the Sinian–Cambrian Hanmushan Group. The Longshoushan Group constitutes the regional metamorphic basement and comprises mainly marble, schist, gneiss, and migmatite. It is unconformably overlain by the Dunzigou and Hanmushan groups, which consist predominantly of low-grade metasedimentary rocks, including phyllite, slate, limestone, metasandstone, and diamictite [53]. Paleozoic–Mesozoic sedimentary strata are only locally exposed. The extensive exposure

of basement rocks reduces attenuation of radiometric signals by surficial cover, allowing airborne gamma-ray spectrometry to characterize near-surface radioelement variations among different bedrock units relatively directly.

2.2. Intrusive Rocks and Uranium Mineralization

Caledonian intermediate to felsic intrusive rocks are widely distributed throughout the study area. The Jiling granitic complex, located in the central part of the metallogenic belt, is the largest intrusive complex and consists mainly of fine-grained diorite, fine- to coarse-grained hornblende–biotite granite, and medium- to coarse-grained porphyritic hornblende–biotite granite [54]. Uranium deposits, mineral occurrences, and radioactive anomalies, including those at Xinshuijing, Jiling, and Geminggou, are predominantly situated within or adjacent to this complex, indicating a pronounced spatial association between the granitic intrusions and regional uranium mineralization [55]. However, the magma source of the complex remains debated and may have involved both partial melting of Paleoproterozoic metasedimentary rocks and mixing between crust- and mantle-derived magmas [56]. Granitic intrusions and the metamorphic basement may therefore represent geological units with potentially elevated uranium backgrounds. Accordingly, high airborne eU values primarily reflect lithological background and cannot, in isolation, be regarded as evidence of a uranium source or mineralization.

Published mineralogical research at Jiling documents albitite-hosted uranium mineralization and associated hematitization and carbonate development [7]. Element mass-balance results further identify sodium addition and potassium loss during Na-metasomatism [16]. These observations support the deposit-scale genetic interpretation but do not imply that all associated surface responses should show potassium enrichment.

Xinshuijing and Jiling are representative alkali-metasomatic uranium deposits within the Longshoushan metallogenic belt. Mineralization is hosted primarily by structurally fractured and hydrothermally altered zones within granitic intrusions and is closely associated with albitization, hematitization, and other alkali-metasomatic processes. At Jiling, element mass-balance calculations and geochemical mapping document substantial element redistribution during Na-metasomatism and subsequent uranium mineralization [16]. These findings provide a deposit-scale basis for considering fluid-related uranium redistribution. They do not establish that each negative surface radiometric deviation represents uranium removed during mineralization.

2.3. Structural Controls and Working Metallogenic Framework

The regional fault system exerts a strong control on the spatial distribution of uranium deposits and mineral occurrences. The fault along the northern margin of the Hexi Corridor constitutes a first-order tectonic boundary. Within the study area, NW-trending faults control the overall distribution of the principal geological units, granitic intrusions, and mineralized zones, whereas subsidiary NE-trending faults cross-cut these structures and generate locally enhanced permeability at fault intersections, bends, and fractured zones. On this basis, the NW-trending faults are inferred to have acted as regional pathways for hydrothermal-fluid migration, whereas subsidiary faults and their intersections may have promoted fluid–rock interaction and mineral precipitation by modifying local stress and permeability conditions.

By integrating lithological backgrounds, deposit characteristics, and structural relationships, we propose a working metallogenic framework comprising “potential high-U background geological units–fluid pathways–sites of uranium re-enrichment.” In this framework, granitic intrusions and parts of the metamorphic basement represent geological units with potentially elevated uranium backgrounds; regional faults and subsidiary

structures controlled fluid migration and the distribution of hydrothermal alteration; and fault intersections, structurally fractured zones, and intensely metasomatized domains provided favourable sites for uranium re-enrichment. The following sections evaluate three spatial relationships within this framework: the correspondence between radioelement anomalies and the orientation of major faults, the proximity of relatively U-depleted zones to fault-related fracture zones, and the association of relatively U-enriched zones with fault intersections or structural bends.

3. Data Acquisition and Processing

3.1. Airborne Gamma-Ray Spectrometric Survey

The airborne gamma-ray spectrometric survey was conducted in 2022 over the Xinshuijing–Yushigou area of Longshoushan, Jinchang City, Gansu Province. Given the high elevation and pronounced topographic relief of the study area, an AS350B3e helicopter equipped with an HR-AGS high-resolution airborne gamma-ray spectrometric system was used to conduct terrain-following flights. The system comprises an airborne array gamma-ray detector, an ultramultichannel spectral analyser and processor, a GPS navigation and positioning system, a radar altimeter, and environmental-parameter sensors. GPS time and one-pulse-per-second signals provided a common temporal reference for gamma-ray counts, spatial coordinates, flight altitude, and environmental parameters, ensuring synchronous acquisition of the different data streams.

The high-resolution airborne gamma-ray spectrometric system employs a distributed parallel architecture that simultaneously performs multichannel digital pulse-height analysis, timing analysis, energy-response compensation, automatic spectral stabilization, and spectral correction and synthesis. This architecture enables synchronized spectral-data acquisition, stable energy linearity, and real-time pulse-signal processing under complex geological and operational conditions.

The survey was conducted at a scale of 1:50,000. The main survey lines were oriented approximately north–south, broadly perpendicular to the regional NW-trending structural belt, with a line spacing of 500 m. Tie lines were oriented approximately orthogonal to the main lines and spaced 7 km apart. Subject to flight-safety requirements, the mean terrain clearance was maintained at approximately 100 m to reduce the effects of gamma-ray attenuation and topographic relief on anomaly amplitudes and spatial positioning. The raw spectral data were sequentially subjected to background subtraction, altitude-attenuation correction, Compton-scattering correction, and sensitivity conversion, followed by temporal synchronization with positioning and environmental data. The final products comprised gridded total count (TC), potassium concentration (K), equivalent uranium concentration (eU), and equivalent thorium concentration (eTh), which were used for subsequent statistical analyses and calculation of the composite parameters.

3.2. Ground Gamma-Ray Spectrometry and Lithological Constraints

Ground measurements were conducted using an HD-2002 portable gamma-ray spectrometer to obtain K, eU, eTh, and TC values for the principal geological units. The sampling locations are shown in Figure 1c. In total, 155 lithologically constrained measurements were acquired, including 45 from granite, 15 from quartz diorite, 15 from mafic dykes, 30 from gneiss–schist–phyllite units, 20 from marble, and 30 from Quaternary cover (Table 1). The measurements were grouped by lithology to compare near-surface radiometric backgrounds among geological units and to help assess the lithological dependence of the airborne anomalies. The ground measurements were used solely to constrain lithological backgrounds and provide cross-scale comparisons; they were not used to infer the source of the ore-forming material or the magnitude of uranium fluxes.

Table 1. Mean ground gamma-ray spectrometric values for the sampled lithological and surficial units.

Serial Number	Lithology/Surficial Unit	*n*	Mean eU (ppm)	Mean eTh (ppm)	Mean K (%)	Mean TC (cps)
1	Granite	45	8.71	39.76	4.98	43.82
2	Quartz diorite	15	9.18	38.26	5.11	42.82
3	Mafic dykes	15	5.31	17.99	3.41	27.31
4	Gneiss, schist, phyllite	30	5.48	21.98	3.79	30.40
5	Marble	20	3.19	8.19	1.88	16.97
6	Quaternary sediments	30	6.50	17.39	3.45	27.74

Notes: *n* denotes the number of ground measurement sites. eU and eTh are equivalent concentrations derived from gamma-ray spectrometry, rather than direct chemical measurements. Values are arithmetic means of the measurements within each sampled unit.

The 155 measurement sites were selected using a purposive lithology-stratified sampling strategy, with site selection guided by representativeness of lithological units, accessibility and outcrop freshness criteria. Their distribution across the mapped lithological units is shown in Figure 1c. The numbers of sites differed among units because of variations in outcrop exposure and terrain accessibility. Consequently, the measurements characterize the sampled exposures rather than providing an area-weighted estimate of the regional radiometric background. At each site, measurements were acquired over flat, fresh bedrock outcrops free of soil cover and vegetation, with the detector positioned 1 m above the rock surface, vertically downward and an acquisition time of 300 s. Instrument calibration was based on national radioactive standard sources for K, U, Th, and stability was checked using a built-in check source before daily field work. Repeat measurements were collected at 15% of sites, with relative deviation of K, U, and Th content being less than 5%. Data were processed using cosmic ray, background and dead-time corrections, with spectrum fitting acceptance criteria.

3.3. Radiometric Variables and Composite Parameters

The airborne dataset comprises four primary variables: K, eU, eTh, and TC. Single-element data characterize the spatial distribution of the radiometric field and lithological variability but cannot readily distinguish primary radiometric backgrounds from radioelement redistribution caused by weathering and leaching, hydrothermal alteration, or superimposed mineralization. To reduce the interpretive ambiguity inherent in single-element data, we additionally calculated three ratios, eU/eTh, eU/K, and eTh/K, and derived four composite parameters: expected uranium background (Gu), relative uranium deviation (Hu), U–K relative enhancement index (F), and normalized relative uranium deviation (B). The calculation and interpretive limitations of each parameter are summarized in Table 2.

Table 2. Radiometric variables, calculation schemes, and geological interpretations.

Method Classification	Parameter Name	Mathematical Model	Geological Significance
Single-element parameter	Uranium content Potassium content Thorium content	eU, eTh, K	The regional distribution patterns and changing trends of each element are compared, and the differences in element content are compared to indicate corresponding geological information.
Single-element ratio parameter	Uranium to thorium ratio Uranium to potassium Ratio Thorium to potassium Ratio	$eU/eTh, eU/K, eTh/K$	Changes in element ratios can indicate weathering, depositional environment, mineralization and other specific geological processes.
Multi-element combination parameters	Expected uranium background (Gu)	$G_{u,i} = rl(i)eTh_i$	The stratigraphic background value is used to identify potential high-uranium background geological units.

Table 2. *Cont.*

Method Classification	Parameter Name	Mathematical Model	Geological Significance
Multi-element combination parameters	Relative uranium deviation (Hu)	$H_{u,i} = eU_i - G_{u,i}$	Represents the deviation of measured eU from the expected uranium background. Positive and negative values indicate eU above and below the estimated lithological background, respectively; they do not directly quantify uranium gain, loss, or transport.
Multi-element combination parameters	U–K relative enhancement index (F)	$F_i = eU_iK_i/eTh_i$	Highlights variations in K and eU relative to eTh; potentially supports alteration interpretation when independently constrained by geology and mineralogy.
Multi-element combination parameters	Normalized relative uranium deviation (B)	$B_i = H_{u,i}/G_{u,i}$	Characterizes the magnitude of change in relative uranium deviation relative to the expected uranium background and is used to compare the relative loss or increase response of different regions.

Let i denote a grid cell and $l(i)$ its mapped lithological unit. For each lithological unit l, individual eU/eTh ratios were first calculated for all valid grid cells. Cells were excluded if eTh was below the instrumental detection limit or 0.5 ppm, or if the relative uncertainty in eTh exceeded 30%. The $1.5 \times IQR$ rule was then applied to the eU/eTh ratios within each lithological unit. Ratios outside the interval $[Q_1 - 1.5 \times IQR, Q_3 + 1.5 \times IQR]$ were excluded from the reference set S_l.

The lithology-specific reference coefficient rl was defined as the median eU/eTh ratio of the retained cells:

$$rl = median_{j \in S_l}\left(\frac{eU_j}{eTh_j}\right)$$

rl is a unit-level reference coefficient rather than the ratio observed at grid cell i. The expected uranium background at cell i was calculated as:

$$G_{u,i} = rl(i)eTh_i$$

The relative uranium deviation Hu, i, normalized relative uranium deviation Bi, and U–K relative enhancement index Fi were calculated as:

$$H_{u,i} = eU_i - G_{u,i}$$

$$B_i = H_{u,i}/G_{u,i}$$

$$F_i = eU_iK_i/eTh_i$$

Both Gu and Hu are expressed in ppm, whereas B is dimensionless. Potassium was entered as its numerical concentration in percent when calculating F; consequently, the numerical scale of F depends on this convention.

Positive and negative Hu values indicate measured eU values above and below the estimated lithological background, respectively. These deviations describe relative enrichment or depletion with respect to the adopted background model. They do not directly quantify uranium addition, removal, or transport. For positive Gu, B necessarily has the same sign as Hu and expresses the same deviation relative to the estimated background.

The F index represents the combined variation of K and the eU/eTh ratio. Elevated F values may result from increased K, increased eU, decreased eTh, or combinations of these changes.

For each geological unit, the number of valid grid cells, arithmetic mean, sample standard deviation, median, skewness, and kurtosis were calculated for the airborne eU, eTh, and K data. The median was included because several lithological populations exhibit

asymmetric or heavy-tailed distributions. Skewness was used to characterize distributional asymmetry, whereas excess kurtosis was used to evaluate the influence of heavy tails and extreme observations. Unless otherwise specified, the descriptive statistics in Table 3 were calculated using all valid grid cells assigned to the corresponding geological unit.

3.4. Retrospective Comparison of Drill-Hole Geological Sections with Airborne Gamma-Ray Spectrometric Anomalies

To strengthen the subsurface geological constraints on the interpretation of airborne gamma-ray spectrometric anomalies, representative drill-hole geological sections from the known Jiling and Xinshuijing uranium deposits were selected for retrospective comparison. The sections show the principal geological features identified by drilling, including ore bodies or mineralized zones, granite, diorite, diabase, and altered rocks. These features were spatially compared with the eU, Gu, Hu, F, and B responses surrounding the surface projections of the deposits. The drill-hole collar locations are also superimposed on the radiometric parameter maps. This comparison shows their plan-view positions relative to the mapped radiometric patterns and complements the subsurface geological sections. Collar locations are distinguished from the surface projections of mineralized intersections, particularly for inclined drill holes.

The Jiling drill-hole section shows that the ore bodies or mineralized zones occur mainly within structurally fractured and altered domains in granitic–dioritic rock associations and are locally influenced by dykes and lithological contacts. The area surrounding the surface projection of the deposit is characterized by generally high eU and Gu values, indicating a pronounced granitic control on its radiometric background. Superimposed on this background, locally negative Hu values occur adjacent to positive Hu values, F is enhanced near some structurally fractured and altered zones, and B further highlights the magnitude of the relative uranium deviations. This parameter assemblage indicates that the Jiling deposit occurs not only within a regionally elevated radiometric background but also in an area characterized by local variations in U–Th–K proportions and relative uranium deviations.

The Xinshuijing drill-hole section indicates that the ore bodies or mineralized zones are concentrated mainly within structurally fractured and hydrothermally altered zones hosted by granitic rocks and are closely associated spatially with dioritic rocks, diabase dykes, and altered rock bodies. The area surrounding their surface projections likewise exhibits elevated eU and Gu values. However, the high-eU zone is relatively extensive and does not correspond precisely to the location of mineralization. By comparison, Hu, F, and B exhibit more localized variations: negative Hu zones occur adjacent to positive deviations, enhanced F values show a close spatial correspondence with structurally controlled alteration zones, and positive B anomalies highlight local uranium increases relative to the lithological background.

The two known deposits display broadly consistent multi-parameter response patterns. Their ore bodies or mineralized zones occur where elevated lithological radiometric backgrounds coincide with structural deformation and hydrothermal alteration. Whereas eU alone primarily reflects the regional radiometric background, the combined Gu, Hu, F, and B responses further reveal variations in radioelement proportions superimposed on that background. Overall, the parameter assemblage comprising elevated eU and Gu values, locally negative Hu values, adjacent positive Hu or B anomalies, and enhanced F values shows a close spatial association with lithological contacts, structurally fractured zones, hydrothermal alteration, and mineralization identified by drilling. This assemblage therefore provides a reference pattern for subsequent candidate-target screening and ground verification.

Table 3. Descriptive statistics and distribution characteristics of airborne gamma-ray spectrometric parameters for the principal geological units in the study area.

No.	Geological Unit	*n*	eU, Mean ± SD (ppm)	eU, Median	eTh, Mean ± SD (ppm)	eTh, Median	K, Mean ± SD (%)	K, Median	eU/eTh	eU/K	eTh/K	eU Skewness	eU Kurtosis
1	Quaternary sediments	3059	3.94 ± 0.69	4.01	10.28 ± 1.46	10.37	2.01 ± 0.18	2.00	0.38	1.96	5.15	0.43	1.86
2	Neogene strata	820	3.68 ± 0.93	3.73	9.63 ± 1.84	9.59	1.92 ± 0.24	1.91	0.38	1.91	5.04	0.18	2.18
3	Jurassic sedimentary rocks	80	2.87 ± 0.79	2.63	6.91 ± 1.25	6.18	1.45 ± 0.25	1.40	0.41	1.97	4.78	0.39	−0.30
4	Proterozoic metamorphic basement	1218	3.97 ± 1.65	3.99	6.42 ± 2.02	6.76	1.47 ± 0.70	1.51	0.61	2.68	4.31	0.62	−0.99
5	Cambrian carbonate sequences	121	4.27 ± 1.21	4.31	10.75 ± 2.80	10.42	2.03 ± 0.27	2.01	0.39	2.09	5.31	0.26	−0.05
6	Sinian siliceous and clastic formations	2781	3.22 ± 1.23	2.97	7.75 ± 2.88	7.66	1.62 ± 0.52	1.70	0.41	1.98	4.85	0.63	1.45
7	Granite	1709	6.01 ± 3.10	6.05	15.12 ± 6.93	14.72	2.38 ± 0.50	2.25	0.39	2.52	6.36	4.56	34.91
8	Quartz diorite	367	4.67 ± 1.07	4.58	12.83 ± 2.85	12.47	2.37 ± 0.31	2.31	0.36	1.96	5.35	0.23	−1.34
9	Mafic dykes	30	5.89 ± 0.94	5.79	14.04 ± 2.10	14.15	2.25 ± 0.43	2.30	0.42	2.61	6.19	5.51	41.30
10	Entire study area	10,185	4.13 ± 1.92	3.98	10.53 ± 4.62	10.30	1.96 ± 0.52	1.98	0.39	2.11	5.38	4.48	53.02

Note: eU and eTh denote equivalent uranium and equivalent thorium concentrations, respectively, derived from airborne gamma-ray spectrometric measurements; they do not represent direct chemical determinations of U and Th. The sample number (*n*) represents the number of valid airborne grid cells assigned to each geological unit. SD denotes the sample standard deviation. Kurtosis is reported as excess kurtosis. Because some geological units show strongly skewed and heavy-tailed distributions, the median should be considered together with the mean and standard deviation when evaluating their representative radioelement concentrations.

4. Results

4.1. Characteristics of the Regional Radiometric Field

K, eU, eTh, and total count (TC) exhibit pronounced spatial heterogeneity across the study area (Figure 2). The regional mean concentrations of K, eU, and eTh are 1.96%, 4.12 ppm, and 10.53 ppm, respectively. High- and low-value zones of these variables generally follow a NW-trending pattern consistent with the regional structural grain of the Longshoushan uplift belt. Calculated from all 10,185 valid grid cells across the study area, the regional eU distribution has a skewness of 4.48 and an excess kurtosis of 53.02 (Table 3). These values indicate a strongly right-skewed and heavy-tailed distribution in which a small number of unusually high eU values exert a disproportionate influence on the regional mean and standard deviation. Consequently, the regional statistics are strongly influenced by a small number of locally elevated values. The use of a uniform regional mean or threshold for anomaly identification may therefore overemphasize geological units with intrinsically high radioactivity while obscuring local variations developed under different geological backgrounds.

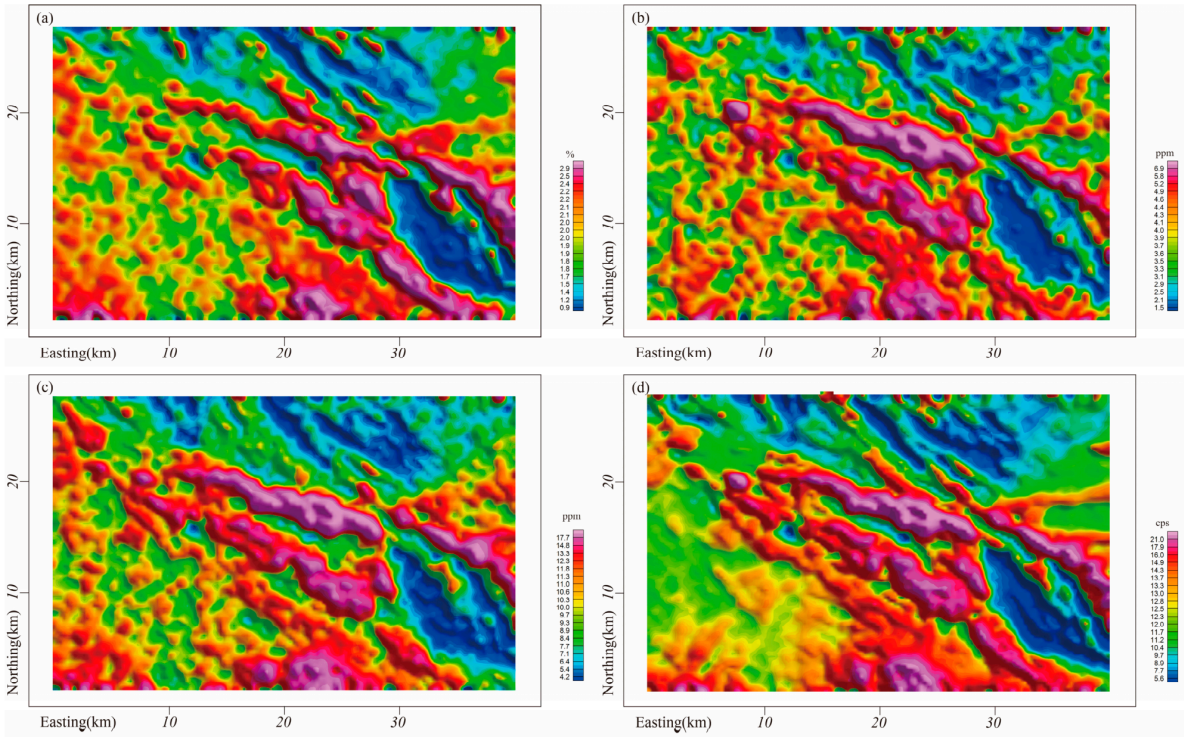

Figure 2. Spatial distributions of airborne gamma-ray spectrometric variables in the study area: (**a**) K, (**b**) eU, (**c**) eTh, and (**d**) total count (TC).

Elevated K values occur mainly within and adjacent to granitic intrusions, reflecting lithological backgrounds rich in K-bearing minerals. Parts of the metamorphic basement and intermediate to felsic intrusive units also exhibit moderate-to-high K responses. Elevated eTh values show a relatively stable spatial distribution and correspond closely to granitic intrusions and parts of the pre-Sinian metamorphic basement, suggesting that the thorium response is controlled primarily by protolith composition and lithological distribution. Elevated eU values generally coincide with high-eTh zones, although their spatial variations are more localized. In some areas, the boundaries and amplitudes of the eU anomalies do not fully correspond to those of eTh, indicating a degree of spatial decoupling between uranium and the thorium-defined background. TC integrates the radiometric contributions of K, eU, and eTh. Its high-value zones occur predominantly

along granitic intrusions and the metamorphic basement, thereby delineating the overall regional radiometric background.

Statistics for the individual geological units further demonstrate the strong lithological dependence of the regional radiometric field. Granite has the highest mean eU and eTh concentrations, at 6.01 and 15.12 ppm (Table 3), respectively. Quartz diorite and mafic dykes generally display the next-highest values, whereas Jurassic sedimentary rocks, Quaternary sediments, and parts of the Sinian successions exhibit comparatively lower radiometric responses. K, eU, eTh, and TC vary among the geological units to different degrees, indicating that the regionally elevated radiometric field primarily reflects the composition of the granitic intrusions and metamorphic basement. Local radiometric anomalies should therefore be evaluated within the same or comparable lithological backgrounds rather than being identified solely from their absolute values across the entire study area. The mapped mafic-dyke unit has higher airborne mean eU and eTh values than quartz diorite. However, the ground measurements show the opposite ordering for these two sampled lithologies (Table 1). The airborne values should therefore not be interpreted directly as the intrinsic composition of unaltered mafic rocks. Possible explanations include contributions from adjacent rocks within the airborne footprint, interpolation across narrow dykes, and differences between the ground-sampling locations and airborne coverage. Local alteration or lithological misclassification may also contribute, but these possibilities require independent verification. The contrast illustrates the need to distinguish map-unit radiometric responses from rock-specific concentrations.

The lithology-specific statistics in Table 3 show that several eU distributions depart markedly from symmetry. In particular, granite and mafic dykes exhibit pronounced positive skewness and high kurtosis, indicating that most grid cells have moderate eU concentrations, whereas a comparatively small number of cells contain substantially elevated values. Consequently, the arithmetic mean and standard deviation of these units are sensitive to a small number of high-value observations and may not represent the concentrations typical of most cells. The corresponding medians, sample sizes, and distribution shapes should therefore be considered together with the mean values when comparing the radiometric characteristics of different geological units.

Although lithology controls the first-order pattern of the regional radiometric field, local radiometric responses do not always coincide with mapped geological boundaries. In and east of the Jiling area, the extent of elevated TC values corresponds closely to the mapped granitic outcrops, indicating that the radiometric field is dominated by the granitic background. In the Xinshuijing area, by contrast, the high-TC zone is smaller than the exposed granitic body, demonstrating that radiometric responses are heterogeneous even within the same intrusion. Some granitic outcrops in the northwestern part of the study area lack corresponding TC highs, whereas several lithological contacts and fault-adjacent areas exhibit localized responses that differ from the regional background. These observations indicate that lithological background explains the overall distribution of the regional radiometric field but does not fully account for the extent and intensity of local anomalies. These local variations may reflect within-unit compositional heterogeneity, hydrothermal alteration, weathering, erosion, or differences in surficial cover. Structural fracturing may influence these processes by modifying permeability or exposure. However, the airborne radiometric data alone cannot distinguish their individual contributions. These mechanisms are therefore considered possible explanations rather than demonstrated causes.

4.2. Correlations and Coupling Among Radiometric Parameters

Overall, eU, eTh, K, and total count (TC) are positively correlated, although the strength of their coupling varies markedly (Figure 3). TC shows its strongest reported

bivariate correlation with eTh (r = 0.86). This association indicates similar spatial variation but does not establish the fraction of TC attributable to thorium. TC integrates radiation across its acquisition energy range, whereas the elemental estimates are derived through spectral processing and calibration. Shared lithological controls and covariance among K, eU, and eTh also affect these correlations. A moderately strong positive correlation occurs between eU and eTh (r = 0.81), reflecting their shared lithological control, whereas the scatter around this relationship indicates localized decoupling of U from Th, potentially associated with uranium mobilization or enrichment. K is moderately correlated with eTh (r = 0.68), whereas the K–eU correlation is the weakest (r = 0.57). Although K and U therefore exhibit some degree of covariation, their distributions may also be influenced by multiple factors, including protolith composition, potassic alteration, and fluid activity. The Spearman correlation coefficients are generally consistent with the corresponding Pearson coefficients, indicating that these relationships are not driven solely by a small number of extreme values.

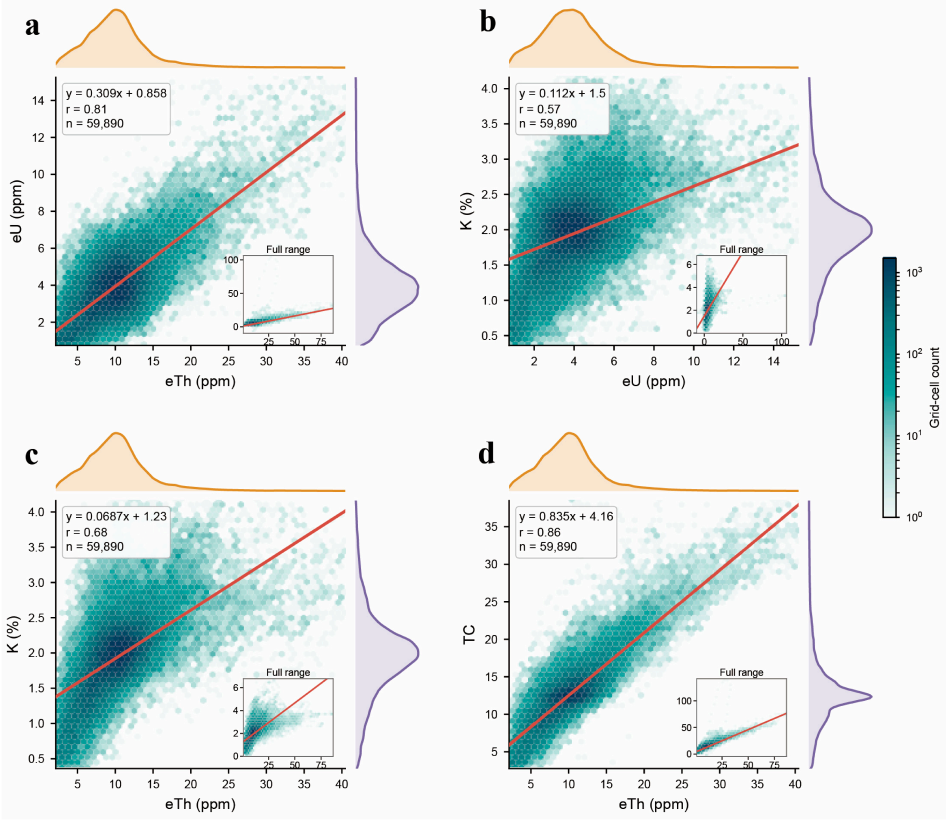

Figure 3. Bivariate relationships among airborne gamma-ray spectrometric variables: (**a**) eU–eTh, (**b**) eU–K, (**c**) K–eTh, and (**d**) TC–eTh.

The parameter correlations decrease in the order TC–eTh > eU–eTh > K–eTh > K–eU. This pattern indicates that the radiometric field is controlled primarily by the regional lithological background, whereas U and K exhibit more pronounced signatures of subsequent redistribution. Accordingly, elevated TC or single-element values should not be interpreted directly as uranium-mineralization anomalies. Exploration interpretation should instead focus on grid cells that deviate from the regional background relationships, including those characterized by high eU/eTh ratios, positive residuals from the eU–eTh regression, and spatial coincidence with K anomalies. These composite anomalies may indicate uranium enrichment superimposed on the lithological background more effectively than high eU values alone, although their geological significance must still be evaluated against lithological, structural, and alteration constraints.

Correlation heatmap analysis reveals pronounced covariation among the primary radiometric parameters in the study area (Figure 4a). The eU/eTh ratio is only weakly correlated with K, eU, and eTh (r = −0.08 to 0.23), indicating that this ratio is relatively insensitive to their absolute concentrations and can, to some extent, highlight the preferential enrichment of U relative to Th.

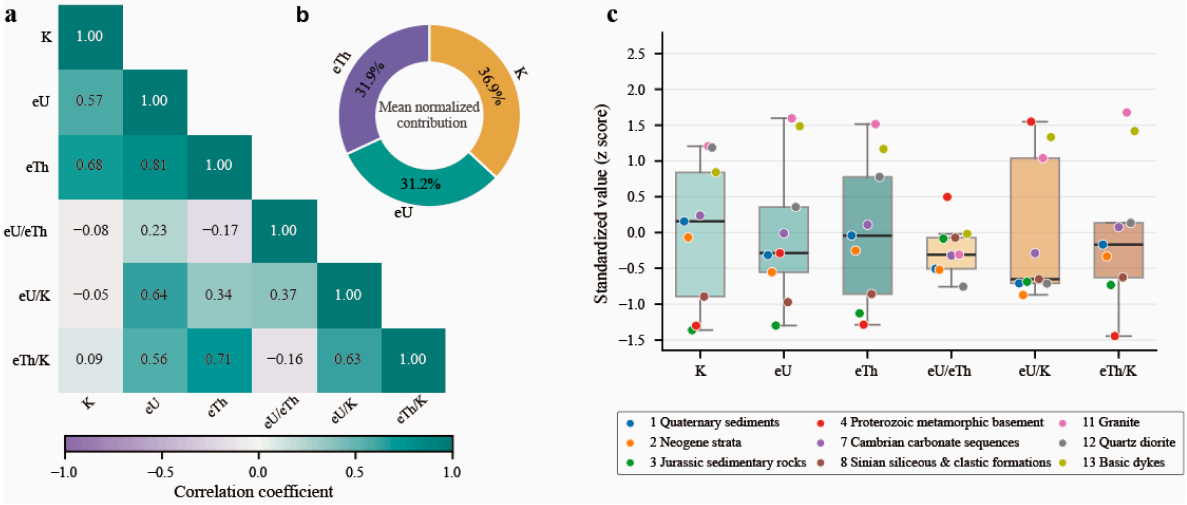

Figure 4. Correlation heat map of radioactive parameters in the study area, range-normalized relative proportions and standardized response characteristic map of different geological units. (**a**) Correlation coefficient matrix of K, eU, eTh, TC and their ratio parameters; (**b**) relative proportions of range-normalized K, eU, and eTh; (**c**) normalized distribution of K, eU, eTh and their ratio parameters in different geological units.

The normalized relative-contribution analysis shows that K, eU, and eTh account for mean proportions of 36.9%, 31.2%, and 31.9%, respectively (Figure 4b). The range-normalized proportions are broadly balanced, but they should not be interpreted as physical or statistical contributions of K, eU, and eTh to TC. These proportions were derived using range normalization of the individual variables and represent only their relative contributions to the observed radiometric response; they do not correspond to the actual mass abundances of the elements.

The standardized parameters vary markedly among geological units (Figure 4c). Granite and mafic dykes generally exhibit elevated K, eU, and eTh responses, reflecting their relatively high regional radiometric backgrounds. Quartz diorite also shows elevated single-element concentrations, although its ratio parameters do not increase correspondingly. The Proterozoic metamorphic basement has a markedly higher eU/eTh ratio than the other units despite its comparatively low absolute K, eU, and eTh concentrations, indicating possible preferential enrichment of U relative to Th within this unit. In contrast, the parameters of most sedimentary and carbonate units are close to or below the regional averages.

The median-normalized K–eU–eTh ternary density distribution is concentrated mainly near the centre of the ternary diagram (Figure 5), indicating that the three radioelements exhibit broadly balanced covariation relative to their respective regional backgrounds across most grid cells. The high-density region extends slightly towards the eU–eTh side, reflecting the comparatively strong coupling between uranium and thorium and supporting the results of the correlation analysis. A small number of samples deviate towards the eU, eTh, or K end-members, indicating varying degrees of selective radioelement enrichment in localized areas. In particular, samples displaced towards the eU end-member may represent anomalous uranium enrichment relative to K and Th and therefore constitute important targets for subsequent identification of relative uranium enrichment.

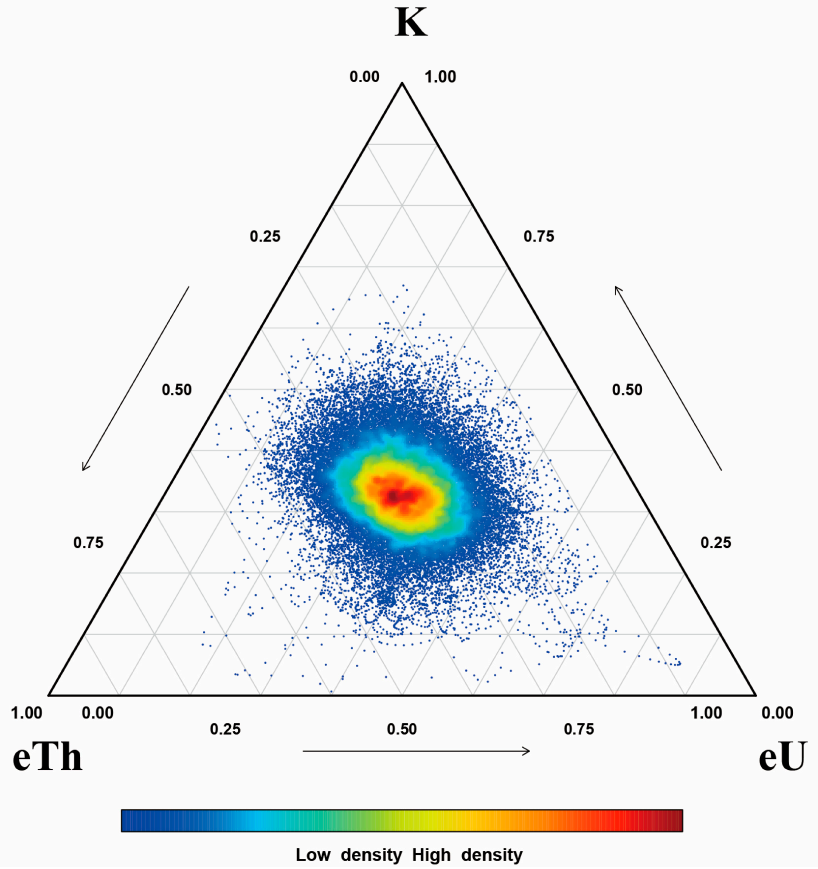

Figure 5. Ternary density distribution diagram of relative composition of K–eU–eTh.

The dominant ternary composition reflects the common lithological control on K, U, and Th across the study area, whereas samples outside the principal density field may record radioelement decoupling associated with later fluid activity, alkali metasomatism, or uranium mobilization.

4.3. Expected Uranium Background and Relative Uranium Deviations

High Gu values occur mainly within granitic intrusions and exposed metamorphic basement in the central and southern parts of the study area. Their spatial distribution broadly inherits the pattern of eTh and lithologies characterized by elevated radiometric backgrounds (Figure 6).

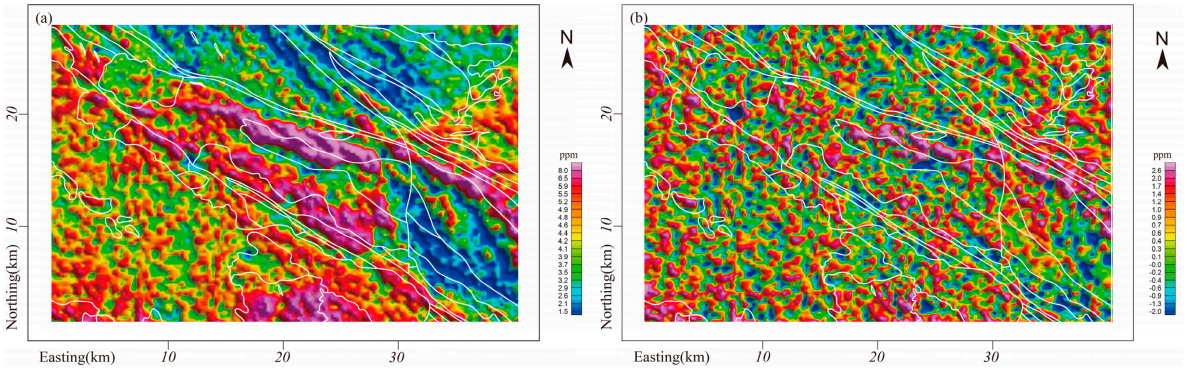

Figure 6. Spatial distribution map of expected uranium background and relative uranium deviation in the study area (the white line is the boundary of the geological unit). (**a**) Expected uranium background (Gu); (**b**) uranium deviation (Hu). White lines indicate mapped geological boundaries.

Positive Hu values indicate eU above the estimated lithological background, whereas negative values indicate eU below that background. These are descriptive relative enrichment and depletion terms, rather than evidence of quantified uranium gain or loss. A non-zero Hu value is not automatically a statistically significant anomaly. Statistical significance requires an explicit uncertainty model and decision criterion. Where such a criterion has not been established, the mapped values are described as positive or negative deviations. Gu denotes the expected uranium background under the adopted reference relationship. It should not be equated with the original pre-alteration uranium concentration, which is not reconstructed by this analysis.

4.4. Responses of Alteration and Relative-Enrichment Parameters

High F values occur mainly along the margins of known deposits and at regional fault intersections, forming an overall NW-trending, belt-like distribution. Some high-F zones spatially overlap with enhanced K-related parameters and elevated eU/eTh ratios, indicating synchronous variations in K–U–Th proportions in these areas.

B further characterizes the magnitude of Hu relative to Gu. Spatial gradients from negative to positive B values occur near the known deposits, although peak B values do not coincide completely with the known ore bodies in all areas. F and B therefore record variations in radioelement proportions and relative uranium deviations constrained by the lithological background and should not be used independently as diagnostic indicators of ore bodies.

The spatial combination of Gu, Hu, F, and B distinguishes three principal response types. The association of high Gu with negative Hu represents relative uranium depletion under an elevated-background condition. Positive Hu and B values indicate measured eU exceeding its expected background, whereas high F values highlight anomalous K–U–Th proportions. Compared with high eU values alone, the integrated parameters provide three complementary perspectives: lithological background, relative uranium deviation, and radioelement-proportion variation (Figure 7).

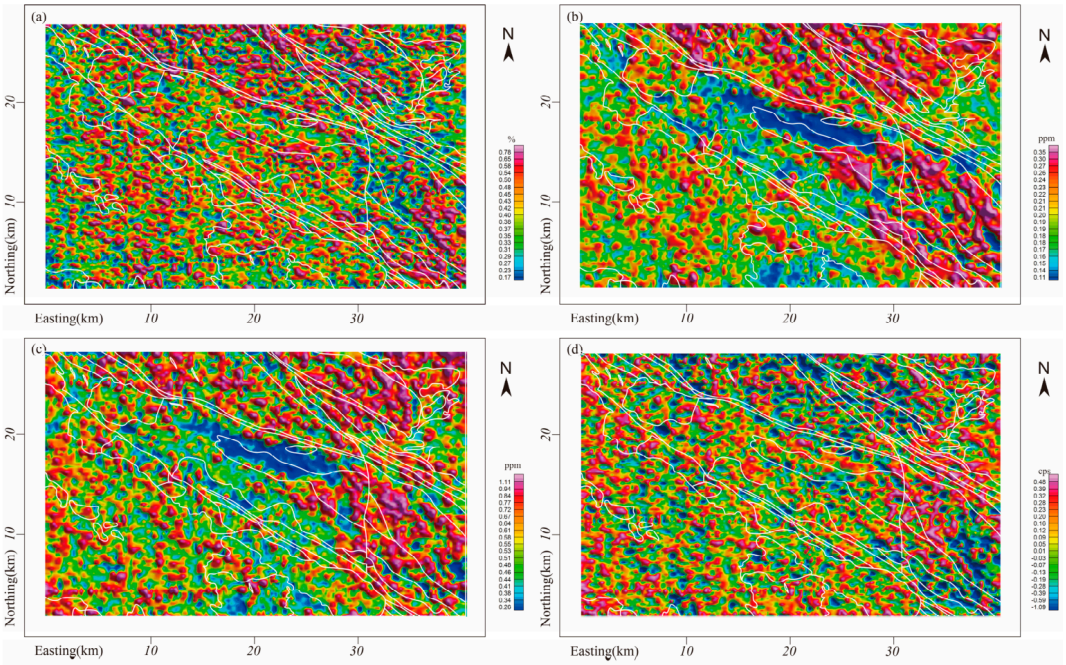

Figure 7. Spatial distribution map of radioactive element ratio parameters and deviations between ratio parameters and normalized relative uranium in the study area (the white line is the boundary of the geological unit). (**a**) eU/eTh; (**b**) K/eTh; (**c**) K/eU; (**d**) B. White lines indicate mapped geological boundaries.

4.5. Single-Element Classification and Multi-Parameter Comprehensive Anomalies

Each radiometric variable was classified using its mean $\overline{x}$ and sample standard deviation σ, calculated over the full set of valid airborne grid cells within the study area. Five non-overlapping classes were defined: low ($< \overline{x} - 2\sigma$), moderately low (($\overline{x} - 2\sigma$ to $\overline{x} - \sigma$), background ($\overline{x} - \sigma$ to $\overline{x} + \sigma$), moderately high ($\overline{x} + \sigma$ to $\overline{x} + 2\sigma$), and high ($> \overline{x} + 2\sigma$). Because the radiometric distributions are strongly skewed and heavy-tailed, these classes are used only to describe relative field intensity and are not treated as statistically calibrated mineralization thresholds (Figure 8).

Moderately high and high TC fields generally correspond to granitic intrusions and pre-Sinian strata, although pronounced local deviations occur. East of Jiling, an arcuate high-TC field broadly follows the geometry of the granitic outcrops. At Xinshuijing, the high-TC field covers only part of the granitic intrusion, whereas the narrow, belt-like high-TC field at Geminggou corresponds relatively closely to the boundary of the pre-Sinian strata. Most known uranium deposits, occurrences, and mineralized sites lie within moderately high to high TC fields; however, fields of the same intensity are also widely distributed across non-mineralized lithological units. Comparison with Gu, Hu, F, and B shows that the known deposits are characterized by a combination of an elevated radiometric background, localized relative uranium depletion, variations in radioelement proportions, and adjacent relative uranium increases, rather than by isolated TC or eU peaks.

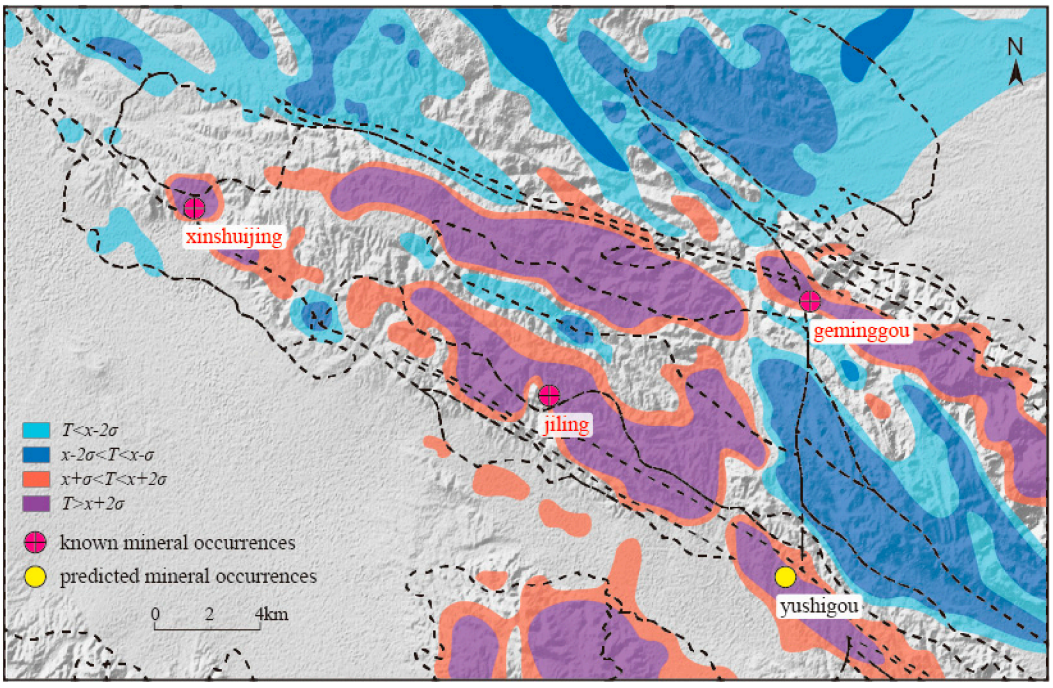

Figure 8. Aerial radioactive field classification map of the study area (the bottom map is a topographic grayscale map; black solid lines represent geological block boundaries).

5. Discussion

The strongly positive skewness and high kurtosis of eU in granite and mafic dykes indicate spatially heterogeneous and heavy-tailed distributions. These characteristics may arise from localized uranium enrichment, variations within the mapped lithological units, mixed responses near geological boundaries, or isolated anomalous grid cells. The extreme values were retained in the descriptive statistics because localized high-eU observations may be relevant to uranium exploration. Nevertheless, they increase the sensitivity of the mean and standard deviation and should not automatically be regarded as representative

lithological background values. For this reason, the mean, median, sample size, and distribution shape are considered jointly, and robust screening is applied when estimating the lithology-specific eU–eTh background relationships.

5.1. Relationships Between Airborne Gamma-Ray Spectrometric Anomalies and Drill-Hole Geology at Known Deposits

The Xinshuijing and Jiling deposits both occur within regionally moderately high to high radiometric fields, although their surface responses are not expressed as isolated eU peaks. The areas surrounding the surface projections of both deposits exhibit elevated radiometric backgrounds and enhanced F values, accompanied by locally negative Hu values that transition spatially towards adjacent positive Hu or B zones. The drill-hole geological sections further show that the ore bodies or mineralized zones at Jiling and Xinshuijing are hosted by granitic–dioritic rock associations and occur in spatial association with dykes, altered rocks, and complex lithological contacts (Figure 9). The co-occurrence of subsurface mineralization, structurally controlled alteration, and multi-parameter surface deviations provides a more explicit geological reference for interpreting the airborne anomalies than simple two-dimensional spatial overlap alone. Figure 10A–H provides a direct map-based comparison between the drill-hole locations and the radiometric parameter patterns at Xinshuijing and Jiling. The overlays complement the geological sections in Figure 9 by showing the surface spatial context of the drilling. Their combined interpretation supports a retrospective assessment of the geological plausibility of the parameter assemblages.

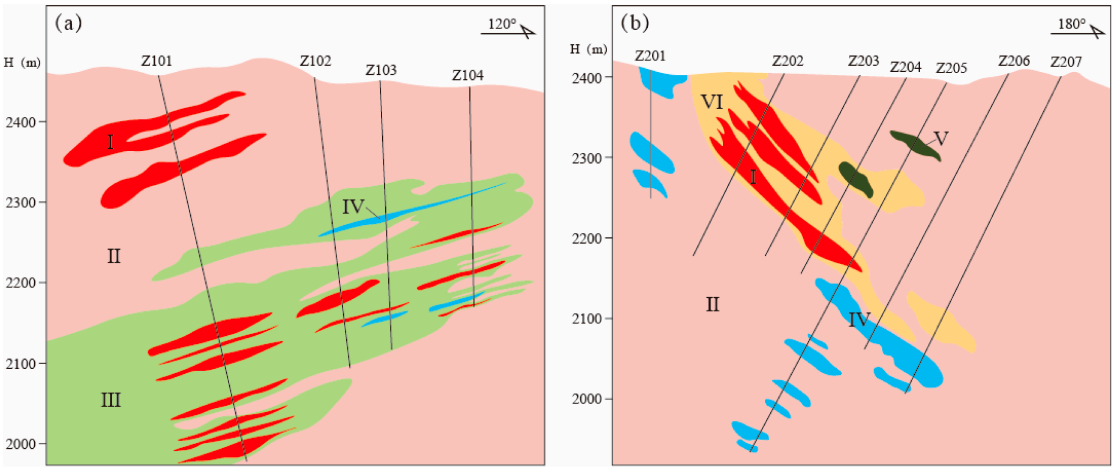

Figure 9. Geological map of drilling sections of known uranium deposits (**a**) Jiling; (**b**) Xinshuijing (I—ore body; II—granite; III—diorite; IV—mineralized body; V—diabase; VI—altered rock body).

These relationships do not, however, demonstrate that any individual parameter is unique to uranium deposits. High Gu values primarily represent lithologies with elevated radiometric backgrounds; F may be jointly influenced by U, K, and low eTh values; and Hu and B depend on the estimation of the expected background. Moreover, subsurface ore bodies identified by drilling do not necessarily produce directly corresponding radiometric peaks at the surface. Whether mineralization produces a detectable airborne response depends on its depth, near-surface extent, uranium concentration, decay-series equilibrium, and the thickness and composition of overlying materials. Ore-body geometry, detector height, and the spatial footprint of the measurement further influence anomaly amplitude. For exposed or very shallow mineralization, thickness and lateral extent may affect the measured response. For deeply buried mineralization, a higher grade or greater thickness does not overcome strong gamma-ray attenuation by overburden. Any associated surface anomaly would require a shallow expression, such as exposed alteration or redistributed

radioactive material. The present data do not establish a transport connection between buried ore bodies and the observed surface deviations. Figure 9 therefore demonstrates retrospective geological consistency at known deposits rather than directly calibrating the capability of airborne parameters to detect deeply buried ore bodies. The exploration interpretation becomes more strongly constrained only when multi-parameter variations occur, at an appropriate spatial scale, in association with structures, alteration, and drilling-confirmed mineralization. Lithological boundaries, variations in weathering, surficial-cover conditions, and gridding effects remain alternative explanations that must be evaluated.

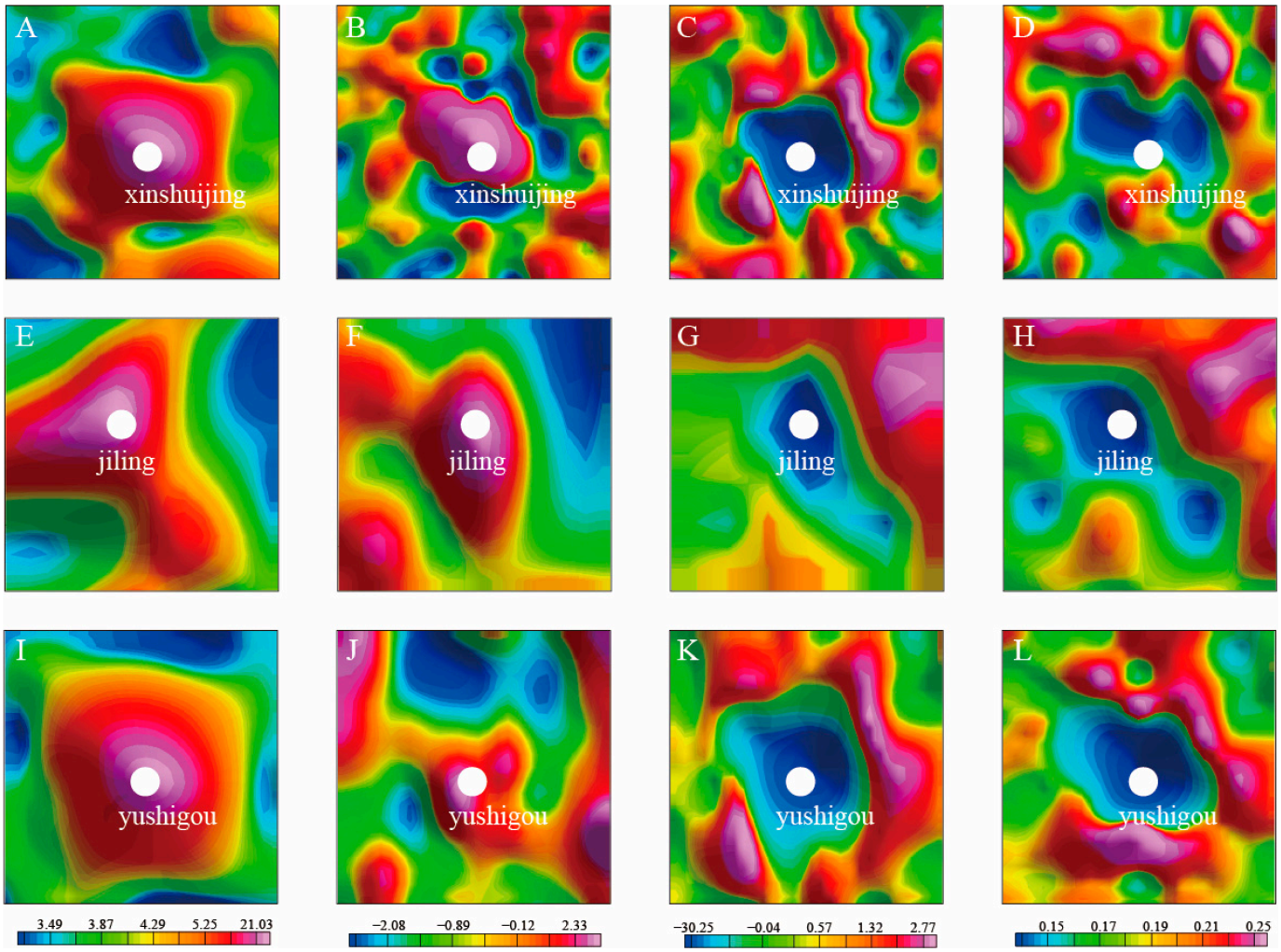

Figure 10. Spatial comparison of airborne radiometric parameters with drill-hole locations at Xinshuijing and Jiling, and the Yushigou candidate target. Columns show eU, F, Hu, and B, respectively. Rows correspond to Xinshuijing (**A**–**D**), Jiling (**E**–**H**), and Yushigou (**I**–**L**). White circles mark drill-hole collar locations, red symbols mark the known deposit locations, and the yellow symbol marks the Yushigou candidate target.

Background uncertainty propagates directly into both Hu and B. For fixed measured eU, a perturbed background $Gu' = (1+\delta)Gu$ gives $Hu' = Hu - \delta Gu$ and $B' = (B-\delta)/(1+\delta)$. Consequently, small deviations may change sign when the reference background changes. Large normalized deviations also require caution where the estimated background is small. Uncertainty arises from the selected reference population, within-unit compositional variability, lithological assignment, and radiometric measurement errors.

The spatial associations described here are based on mapped proximity and visual comparison, rather than formal tests of spatial dependence. Their interpretation is limited by survey spacing, the radiometric footprint, geological-map accuracy, and interpolation. Fine grid spacing does not provide spatial resolution equivalent to the grid-cell size. Consequently, apparent alignment with individual faults or narrow alteration zones should be interpreted at the effective survey scale.

5.2. Yushigou Candidate Exploration Target

Yushigou is identified as an analogy-based candidate exploration target. Its mapped setting combines proximity to a granitic intrusion and a NW-trending fault with elevated F and neighbouring negative and positive uranium deviations. These features resemble aspects of the patterns observed around Xinshuijing and Jiling. The interpretation is qualitative and does not rely on an independently calibrated mineralization threshold. The statistical classes used to display the radiometric fields are not validated criteria for confirming uranium mineralization. Yushigou therefore requires independent evaluation through ground radiometry, rock geochemistry, alteration mapping, and, where justified, drilling.

Figure 10 further shows that Xinshuijing, Jiling, and Yushigou exhibit similar, although not identical, spatial responses across the four airborne gamma-ray spectrometric parameters. Both Xinshuijing and Jiling occur within areas of elevated eU background. Hu and B show locally negative deviations near the deposit and drill-hole projection locations, with positive deviations occurring in surrounding or adjacent areas, thereby forming spatial gradients from relative depletion to relative enrichment. F exhibits localized enhancement and pronounced spatial heterogeneity. At Yushigou, eU forms a relatively concentrated local high, while negative Hu and B deviations occur near the centre of the target and are surrounded by positive deviations. F also varies markedly within and around the target area. The three sites therefore share a parameter assemblage characterized by an elevated eU background, locally negative Hu and B deviations, peripheral positive deviations, and variations in F. This pattern indicates that the Yushigou anomaly is not defined solely by elevated eU but exhibits a multi-parameter spatial architecture resembling those of the known deposits. Nevertheless, the three sites differ in anomaly magnitude, geometry, and spatial extent. The parameter assemblage at Yushigou therefore provides only an analogy-based criterion for target screening, and its exploration significance requires further evaluation through ground gamma-ray spectrometry, rock geochemistry, alteration mapping, and engineering verification.

5.3. Spatial Relationship Between Structure, Alteration and Nuclide Redistribution

The anomalies in the study area are generally distributed along the northwest-trending structure and are locally enhanced at the intersection or turning point of the northwest-trending main fault and the northeast-trending secondary fault. Borehole profiles at Jiling and Xinshuijing show that ore bodies or mineralized bodies, granitic–dioritic surrounding rocks, dikes and altered intrusive bodies form a complex underground space combination, providing a geological background for structural fragmentation and fluid–rock reaction to participate in mineralization. The underground structure is spatially compatible with the multi-parameter deviation of the deposit's surface projection neighborhood, but the existing data have not established a direct causal link between the fault activity period, the deep ore body and the near-surface radioactive response.

Combining the lithology distribution, parameter fields and mineralization–alteration relationships revealed by drilling, a working model of "potential high uranium background—possible structural channels—candidate relative increase locations" to be independently verified can be proposed: granite rock bodies and partially metamorphic

basement provide a higher radioactive background; faults, dikes and altered rock bodies may constitute fluid migration and water–rock reaction spaces; the overlap of Hu- or B-positive relative deviations with favorable structural locations marks the relative increase area that requires further verification. The borehole section strengthens the geological basis for the "structure–alteration–mineralization" link in the model, but Gu, Hu, F and B are still near-surface radioactive proxies and cannot directly determine the material source, migration flux and time sequence.

At the two known deposits, the interpreted surface pattern combines elevated radiometric backgrounds with local uranium deviations and radioelement-ratio variations. The Na-metasomatic geological context is based on the deposit evidence summarized in Section 2.2, rather than inferred from these radiometric parameters alone. This pattern should not be regarded as a universal diagnostic signature of alkali-metasomatic uranium deposits. This combination may explain the lack of known mineralization in some granite highfields, as well as the simultaneous positive and negative relative deviations near the deposits. Compared with fixed single-element thresholds, multi-parameter spatial gradients and their joint constraints with structural and alteration information are more suitable for regional target ranking in complex bedrock areas.

5.4. Limitations of Airborne Radiometric Interpretation

Airborne gamma-ray spectrometry primarily characterizes shallow surface materials and does not directly detect deeply buried uranium ore bodies. Weathering can redistribute uranium and potassium, while transported Quaternary sediments may obscure or replace the radiometric signature of underlying bedrock. Cover thickness and moisture can further modify measured intensities. Terrain and variable ground clearance affect measurement geometry, and altitude correction does not necessarily remove all terrain-related effects.

Equivalent uranium is inferred from decay-product emissions and may differ from chemical uranium where secular equilibrium is disturbed. Negative Hu or B values may therefore reflect surface processes, disequilibrium, or background-model error, rather than hydrothermal uranium removal. The mapped patterns provide near-surface exploration evidence whose relationship to concealed mineralization requires independent verification.

6. Conclusions

This study integrates airborne gamma-ray spectrometry, ground radiometric measurements, geological information, and drill-hole sections to examine uranium-related radiometric patterns in the Xinshuijing–Yushigou area.

(1) The regional radiometric field is strongly influenced by lithology, particularly granitic intrusions and parts of the metamorphic basement. Elevated eU alone therefore cannot distinguish intrinsically radioactive rocks from mineralization-related responses. Local departures from the broader lithological pattern require consideration of compositional variability, alteration, weathering, and cover.

(2) The combined interpretation of Gu, Hu, F, and B separates estimated background levels, uranium deviations, and radioelement-proportion changes. Positive and negative deviations describe present-day eU relative to the selected background; they do not independently establish uranium addition, removal, or transport. The parameters are mathematically related and should not be treated as independent evidence.

(3) Comparisons with Xinshuijing and Jiling identify qualitatively similar parameter assemblages near known mineralization and associated geological features. These comparisons provide retrospective geological support but do not establish independent predictive performance. Yushigou exhibits a comparable mapped assemblage and is proposed as a candidate target for field verification.

(4) The framework provides complementary near-surface information for exploration screening in terrains with variable radiometric backgrounds. Its application remains conditional on background-estimation reliability, measurement quality, surface conditions, and the effective spatial resolution of the survey. Independent field investigations and quantitative spatial evaluation are required to test its exploration value.

Author Contributions: Conceptualization, J.X., Y.M. and Y.L.; methodology, J.X.; software, J.X., Y.M. and Y.L.; validation, J.X., Y.M. and Y.L.; formal analysis, Y.M.; investigation, J.X., Y.M. and Y.L.; resources, Y.M.; data curation, Y.Z. and X.W.; writing—original draft preparation, J.X.; writing—review and editing, Y.M.; visualization, J.X.; supervision, B.W.; project administration, Z.J. and X.Z.; funding acquisition, Z.J. All authors have read and agreed to the published version of the manuscript.

Funding: This research was supported by the National Science and Technology Major Project for Deep-Earth Exploration and Mineral Resources (Grant no. 2025ZD1011401), the National Natural Science Foundation of China (Grant no. U2344203), the China Geological Survey project "Integrated Aeromagnetic and Gravity Survey of the Awulale Iron Resource Base, Xinjiang" (Grant no. DD20243247), and the National Key Laboratory of Big Data and Decision (No. DSJ-ZZKY-2025-08).

Data Availability Statement: The original contributions presented in this study are included in the article. Further inquiries can be directed to the corresponding authors.

Conflicts of Interest: The authors declare no conflicts of interest. Jianchun Xu is an employee of the China Aero Geophysical Survey and Remote Sensing Center for Natural Resources. This paper reflects the academic views of the authors and does not represent the official position of the institution.

References

1. Cuney, M.; Emetz, A.; Mercadier, J.; Mykchaylov, V.; Shunko, V.; Yuslenko, A. Uranium deposits associated with Na-metasomatism from central Ukraine: A review of some of the major deposits and genetic constraints. *Ore Geol. Rev.* **2012**, *44*, 82–106. [CrossRef]
2. Mishra, P.; Sati, M.; Krishnamurthi, R. A Review on Uranium Mineralization Related to Na-Metasomatism: Indian and International Examples. *Geosciences* **2024**, *14*, 304. [CrossRef]
3. Zhang, J.D. Review on Research Progress of Uranium-Ore Prospecting Geological Theories in China. *Acta Geol. Sin.* **2012**, *86*, 1489–1498. (In Chinese)
4. Cai, Y.; Zhang, J.; Li, Z.; Guo, Q.; Song, J.; Fan, H.; Liu, W.; Qi, F.; Zhang, M. Outline of uranium resources characteristics and metallogenetic regularity in China. *Acta Geol. Sin. Engl. Ed.* **2015**, *89*, 918–937. [CrossRef]
5. Zhong, J.; Wang, S.Y.; Gu, D.Z.; Cai, Y.Q.; Fan, H.H.; Shi, C.H.; Hu, C.N. Geology and fluid geochemistry of the Na-metasomatism U deposits in the Longshoushan uranium metallogenic belt, NW China: Constraints on the ore-forming process. *Ore Geol. Rev.* **2020**, *116*, 103214. [CrossRef]
6. Zhao, R.Y.; Chen, Y.C.; Chen, Y.J.; Wang, G.; Nie, L.; Rong, X.; Li, T. Geological Characteristics and Its Genesis of the Jiling Na-metasomatic Uranium Deposit in Longshou Mountains, Gansu Province. *Earth Sci.* **2020**, *45*, 90–107. (In Chinese with English abstract).
7. Yu, C.D.; Wang, K.X.; Liu, X.D.; Cuney, M.; Pan, J.Y.; Wang, G.; Zhang, L.; Zhang, J. Uranium Mineralogical and Chemical Features of the Na-Metasomatic Type Uranium Deposit in the Longshoushan Metallogenic Belt, Northwestern China. *Minerals* **2020**, *10*, 335. [CrossRef]
8. Zhong, J.; Li, Z.Y.; Cai, Y.Q.; Yu, H.; Bondarenko, S.; Lin, C.; Cao, Y.; Belskyy, V. The Geological, Geochemical Characteristics and Metallogenic Rules of the Alkaline Metasomatism Uranium Deposits. *World Nucl. Geosci.* **2023**, *40*, 133–151. (In Chinese with English abstract).
9. Dolníček, Z.K.; René, M.; Hermannová, S.; Prochaska, W. Origin of the Okrouhlá Radouň episyenite-hosted uranium deposit, Bohemian Massif, Czech Republic: Fluid inclusion and stable isotope constraints. *Miner. Depos.* **2014**, *49*, 409–425. [CrossRef]
10. Polito, P.A.; Kyser, T.K.; Stanley, C. The Proterozoic, albitite-hosted, Valhalla uranium deposit, Queensland, Australia: A description of the alteration assemblage associated with uranium mineralisation in diamond drill hole V39. *Miner. Depos.* **2009**, *44*, 11–40. [CrossRef]
11. Sharpe, R.; Fayek, M.; Quirt, D.; Jefferson, C.W. Geochronology and Genesis of the Bong Uranium Deposit, Thelon Basin, Nunavut, Canada. *Econ. Geol.* **2015**, *110*, 1759–1777. [CrossRef]
12. Chen, W.; Ni, T. Quantitative Constraints on the Exhumation and Preservation of the Giant Jinchuan Cu-Ni Sulfide Deposit. *J. Earth Sci.* **2026**, *37*, 1540–1551. [CrossRef]

13. Wilde, A.; Otto, A.; Jory, J.; MacRae, C.; Pownceby, M.; Wilson, N.; Torpy, A. Geology and Mineralogy of Uranium Deposits from Mount Isa, Australia: Implications for Albitite Uranium Deposit Models. *Minerals* **2013**, *3*, 258–283. [CrossRef]
14. Abd El Nabi, S.H. Evaluation of airborne gamma-ray spectrometric data for the Missikat uranium deposit, Eastern Desert, Egypt. *Appl. Radiat. Isot.* **2001**, *54*, 497–507. [CrossRef] [PubMed]
15. Zhong, J.; Mihalasky, M.; Cuney, M.; He, S.; Li, J.-J. Unraveling the hydrothermal history of the Xinshuijing Na-metasomatite uranium deposit in the Longshoushan Metallogenic Belt, Northwest China by coupled hydrothermal zircon U-Pb and albite Ar-Ar dating. *J. Earth Sci.* **2026**, *37*, 1131–1151. [CrossRef]
16. Shao, D.; Han, Y.; Wang, G.; Ma, L.; He, J.; Zhao, G. Quantifying element mass transfer in the Jiling Na-metasomatic hydrothermal uranium deposit, Northwest China. *Ore Geol. Rev.* **2024**, *173*, 106247. [CrossRef]
17. Cuney, M. The extreme diversity of uranium deposits. *Miner. Depos.* **2009**, *44*, 3–9. [CrossRef]
18. Jiao, J.; Han, F.; Zhao, L.; Duan, J.; Wang, M. Magnetite Geochemistry of the Jinchuan Ni-Cu-PGE Deposit, NW China: Implication for Its Ore-Forming Processes. *Minerals* **2019**, *9*, 593. [CrossRef]
19. Lobato, L.M.; Fyfe, W.S. Metamorphism, metasomatism, and mineralization at Lagoa Real, Bahia, Brazil. *Econ. Geol.* **1990**, *85*, 968–989. [CrossRef]
20. Turpin, L.; Maruejol, P.; Cuney, M. U-Pb, Rb-Sr and Sm-Nd chronology of granitic basement, hydrothermal albitites and uranium mineralization (Lagoa Real, South-Bahia, Brazil). *Contrib. Mineral. Petrol.* **1988**, *98*, 139–147. [CrossRef]
21. International Atomic Energy Agency (IAEA). *Airborne Gamma Ray Spectrometer Surveying*; Technical Reports Series No. 323; IAEA: Vienna, Austria, 1991.
22. Youssef, M.A.S.; Elkhodary, S.T. Utilization of airborne gamma ray spectrometric data for geological mapping, radioactive mineral exploration and environmental monitoring of southeastern Aswan City, South Eastern Desert, Egypt. *Geophys. J. Int.* **2013**, *195*, 1689–1700. [CrossRef]
23. Raghuwanshi, S.S. Airborne gamma-ray spectrometry in uranium exploration. *Adv. Space Res.* **1992**, *12*, 77–86. [CrossRef]
24. Minty, B.R.S. Fundamentals of airborne gamma-ray spectrometry. *AGSO J. Aust. Geol. Geophys.* **1997**, *17*, 39–50.
25. Dickson, B.L.; Scott, K.M. Interpretation of aerial gamma-ray surveys—Adding the geochemical factors. *AGSO J. Aust. Geol. Geophys.* **1997**, *17*, 187–200.
26. McCafferty, A.E.; Van Gosen, B.S. Airborne gamma-ray spectrometer and magnetic surveys over the United States. *J. Appl. Geophys.* **2012**, *74*, B101–B109.
27. Winkelmann, I.; Thomas, M.; Vogl, K. Aerial measurements on uranium ore mining, milling and processing areas in Germany. *J. Environ. Radioact.* **2001**, *53*, 301–311. [CrossRef] [PubMed]
28. Asfahani, J.; Al-Hent, R.; Aissa, M. Aerial gamma spectrometric survey as a tool for evaluating the uranium remobilization degree: Case study from Al-Awabed area, Northern Palmyrides, Syria. *Appl. Radiat. Isot.* **2008**, *66*, 1262–1274. [CrossRef] [PubMed]
29. Youssef, M.A.S.; Sabra, M.E.M.; Abdeldayem, A.L.; Masoud, A.A.; Mansour, S.A. Uranium migration and favourable sites of potential radioelement concentrations in Gabal Umm Hammad area, Central Eastern Desert, Egypt. *NRIAG J. Astron. Geophys.* **2017**, *6*, 368–378. [CrossRef]
30. Tarshan, A. Detection of Uranium Anomalies and Alteration Zones Using Airborne Gamma-Ray Spectrometry at Gabal Attala and Its Surrounding Area, Eastern Desert, Egypt. *Earth Sci.* **2022**, *11*, 121–129. [CrossRef]
31. Jiang, Z.; Han, X.; Lin, Z.; Hu, H.; Lai, Q.; Gu, Y.; Wu, Z.; Zhao, X. Large-Scale Aerial Gamma Spectroscopy for Exploring Sandstone-Type Uranium Deposits: A Case Study of Gexi Area, Inner Mongolia. *Appl. Geophys.* **2025**, *22*, 672–683. [CrossRef]
32. Siagné, Z.H.; Kouamelan, A.N.; Digbeu, W.; Aïfa, T.; Houssou, N.G.N.; N'dri, K.A.; Gbele, O. Integration of airborne gamma-ray spectrometry and remote sensing data for mapping of gold-bearing structures in the Doropo region, Northeastern Côte d'Ivoire (Southern part of West African Craton). *All Earth* **2025**, *37*, 1–14. [CrossRef]
33. Airo, M.-L.; Loukola-Ruskeeniemi, K. Characterization of sulfide deposits by airborne magnetic and gamma-ray responses in eastern Finland. *Ore Geol. Rev.* **2004**, *24*, 67–84. [CrossRef]
34. Bedini, E.; Rasmussen, T.M. Use of airborne hyperspectral and gamma-ray spectroscopy data for mineral exploration at the Sarfartoq carbonatite complex, southern West Greenland. *Geosci. J.* **2018**, *22*, 641–651. [CrossRef]
35. Mostafaei, K.; Kianpour, M.N.; Yousefi, M.; Saleki, M. Improving the Results of the Fractal Model of Geochemical Mineralization Probability Index Using the Gray Wolf Algorithm on the Stream Sediments Data of Sarduiyeh-Baft Area. *J. Min. Environ.* **2025**, *16*, 1165–1178. [CrossRef]
36. Mostafaei, K.; Kianpour, M. Application of Magnetometry in Manto-Type Copper Deposit Exploration: A Case Study from Meyami, Iran. *Rud.-Geol.-Naft. Zb.* **2022**, *37*, 1–14. [CrossRef]
37. Bonnetti, C.; Liu, X.; Cuney, M.; Mercadier, J.; Riegler, T.; Yu, C. Evolution of the uranium mineralisation in the Zoujiashan deposit, Xiangshan ore field: Implications for the genesis of volcanic-related hydrothermal U deposits in South China. *Ore Geol. Rev.* **2020**, *122*, 103514. [CrossRef]

38. Asfahani, J.; Al-Hent, R.; Aissa, M. Radioactive and geological analysis of airborne gamma spectrometric data for locating favorable traps for uranium prospecting in the Syrian desert (Area-1), Syria. *Appl. Radiat. Isot.* **2012**, *70*, 2317–2327. [CrossRef] [PubMed]
39. Hafeez, T.H.A.; Youssef, M.A.S.; Mohamed, W.H. Utilization of airborne gamma ray spectrometric data for geological mapping and radioactive mineral exploration of Gabel Umm Tineidba area, south eastern desert, Egypt. *World J. Eng.* **2015**, *12*, 149–160. [CrossRef]
40. Elkhadragy, A.A.; Ismail, A.A.; Eltarras, M.M.; Azzazy, A.A. Utilization of airborne gamma ray spectrometric data for radioactive mineral exploration of G.Abu Had—G.Umm Qaraf area, South Eastern Desert, Egypt. *NRIAG J. Astron. Geophys.* **2017**, *6*, 148–161. [CrossRef]
41. Dickson, B.L.; Fraser, S.J.; Kinsey-Henderson, A. Interpreting aerial gamma-ray surveys utilising geomorphological and weathering models. *J. Geochem. Explor.* **1996**, *57*, 75–88. [CrossRef]
42. International Atomic Energy Agency. *Guidelines for Radioelement Mapping Using Gamma Ray Spectrometry*; IAEA-TECDOC-1363; IAEA: Vienna, Austria, 2003.
43. Gnojek, I.; Přichystal, A. A new zinc mineralization detected by airborne gamma-ray spectrometry in northern Moravia (Czechoslovakia). *Geoexploration* **1985**, *23*, 491–502. [CrossRef]
44. Pires, A.C.B.; Carmelo, A.C.; Martins-Ferreira, M.A.C. Statistical enhancement of airborne gamma-ray uranium anomalies: Minimizing the lithological background contribution in mineral exploration. *J. Geochem. Explor.* **2019**, *198*, 100–113. [CrossRef]
45. Xi, Y.; Liu, J.; Wu, S.; Lu, N.; Liao, G.; Li, Y.; Li, F.; Qu, N. The application of airborne gamma-ray spectrometric multi-element composite parameters in the prediction of uranium prospecting areas in Qinling Region, China. *Minerals* **2025**, *15*, 492. [CrossRef]
46. Xiao, W.; Windley, B.F.; Sun, S.; Li, J.; Huang, B.; Han, C.; Yuan, C.; Sun, M.; Chen, H. A tale of amalgamation of three Permo-Triassic collage systems in Central Asia: Oroclines, sutures, and terminal accretion. *Annu. Rev. Earth Planet. Sci.* **2015**, *43*, 477–507. [CrossRef]
47. Tian, R.G.; Zhu, W.; Zhang, J.; Gao, S.; Zhang, B.; Zhao, H.; Li, T. Late Paleozoic Tectonic Evolution of the Paleo-Asian Ocean in the Northern Alxa Block (NWChina). *Tectonics* **2020**, *39*, e2020TC006359. [CrossRef]
48. Song, D.; Xiao, W.; Windley, B.F.; Han, C. Provenance and tectonic setting of late Paleozoic sedimentary rocks from the Alxa Tectonic Belt (NW China): Implications for accretionary tectonics of the southern Central Asian Orogenic Belt. *Bulletin* **2021**, *133*, 253–276. [CrossRef]
49. Zhang, B.; Zhang, J.; Zhao, H.; Qu, J.; Zhang, Y.; Niu, P.; Hui, J.; Yun, L.; Hauzenberger, C. Kinematics and Geochronology of Late Paleozoic-Early Mesozoic Ductile Deformation in the Alxa Block, NW China: New Constraints on the Evolution of the Central Asian Orogenic Belt. *Lithosphere* **2021**, *2021*, 3365581. [CrossRef]
50. Song, S.; Niu, Y.; Su, L.; Zhang, C.; Zhang, L. Continental orogenesis from ocean subduction, continent collision/subduction, to orogen collapse, and orogen recycling: The example of the North Qaidam UHPM belt, NW China. *Earth-Sci. Rev.* **2014**, *129*, 59–84. [CrossRef]
51. Gong, J.; Zhang, J.; Wang, Z.; Yu, S.; Li, H.; Li, Y. Origin of the Alxa Block, western China: New evidence from zircon U–Pb geochronology and Hf isotopes of the Longshoushan Complex. *Gondwana Res.* **2016**, *36*, 359–375. [CrossRef]
52. Xu, J.; Gu, X.; Zhang, Y.; Wang, J.; He, G.; Zhou, C.; Liu, R. Geology, fluid inclusions, H-O isotope, and hydrothermal zircon U-Pb geochronology of the Daqingshan orogenic gold deposit in Beishan orogenic belt, Xinjiang, NW China. *Miner. Depos.* **2021**, *56*, 325–342. [CrossRef]
53. Zhong, J.; Fan, H.H.; Gu, D.Z.; Wang, S.Y.; Chen, J.Y.; Shi, C.H.; Li, H.Q. Major and Trace Element Migration and Metallogenic Processes of the Xinshuijing U-Th Deposit in the Longshoushan Metallogenic Belt, Gansu Province. *Geol. China* **2016**, *43*, 1393–1408. (In Chinese with English abstract). [CrossRef]
54. Wang, K.X.; Yu, C.D.; Yan, J.; Liu, X.D.; Liu, W.H.; Pan, J.Y. Petrogenesis of Early Silurian granitoids in the Longshoushan area and their implications for the extensional environment of the North Qilian Orogenic Belt, China. *Lithos* **2019**, *342–343*, 152–174. [CrossRef]
55. Wang, S.Y.; Fan, H.H.; Gu, D.Z.; Zhong, J.; Chen, J.Y.; Song, J.Y.; Zhu, Q.L.; Wang, G.; Wang, W.; Shao, D.; et al. Uranium Mineral Characteristics and Chronology of the Jiling Deposit in the Longshoushan Uranium Metallogenic Belt. *J. East China Inst. Technol. (Nat. Sci. Ed.)* **2020**, *43*, 501–513. (In Chinese with English abstract).
56. Liu, W.; Liu, X.; Pan, J.; Wang, K.; Wang, G.; Niu, Y.; Gong, W. Magma Mixing Genesis of the Mafic Enclaves in the Qingshanbao Complex of Longshou Mountain, China: Evidence from Petrology, Geochemistry, and Zircon Chronology. *Minerals* **2019**, *9*, 195. [CrossRef]

Disclaimer/Publisher's Note: The statements, opinions and data contained in all publications are solely those of the individual author(s) and contributor(s) and not of MDPI and/or the editor(s). MDPI and/or the editor(s) disclaim responsibility for any injury to people or property resulting from any ideas, methods, instructions or products referred to in the content.